Soft Matter

PAPER

View Article Online
View Journal | View Issue

Cite this: *Soft Matter*, 2022, **18**, 1183

The rheology and foamability of crystal-melt suspensions composed of triacylglycerols†

Kim Mishra, *[a] Fabian Kämpf, [a] Silas Ehrengruber,[a] Julia Merkel,[a] Nico Kummer, [ab] Robin Pauer,[c] Peter Fischer [a] and Erich J. Windhab[a]

The rheology of triacylglycerol (TAG) crystal-melt suspensions (CMSs) consisting of anhydrous milk fat (AMF), cocoa butter (CB), and palm kernel oil (PKO) as function of crystallization shear rate $\dot{\gamma}_{cryst}$ and crystal volume fraction Φ_{SFC} is investigated by in-line ultrasound velocity profiling – pressure difference (UVP-PD) rheometry. Measurements up to Φ_{SFC} = 8.8% are presented. Below the percolation threshold Φ_c, no yield stress τ_0 is observed and the viscosity η scales linearly with Φ_{SFC}. Above Φ_c, a non-linear dependency of both τ_0 and η as function of Φ_{SFC} is apparent. For AMF and CB, the increase in $\dot{\gamma}_{cryst}$ leads to a decrease in η and τ_0 as function of Φ_{SFC}, whereas for PKO based CMSs the opposite is the case. Scanning electron microscopy (SEM) and polarized light microscopy (PLM) relate these rheological findings to the microstructure of the investigated CMSs by taking the effective aspect ratio a_{eff} and the concept of the effective crystal volume fraction Φ_{SFC}^{eff} into account. Foam formation by dynamically enhanced membrane foaming (DEMF) is performed directly after crystallization and reveals that depending on the CMS rheology and crystallite-, crystallite cluster- and crystal floc microstructure, a wide range of gas volume fractions between 0.05–0.6 are achievable.

Received 19th November 2021,
Accepted 28th December 2021

DOI: 10.1039/d1sm01646f

rsc.li/soft-matter-journal

1 Introduction

Crystal-melt suspensions (CMSs) are a class of disperse system where the continuous phase is a melt and the disperse phase a crystalline solid.[1] The melt phase and the crystalline solid phase are related by a thermodynamic equilibrium leading to temperature and pressure dependent phase fractions. Typical CMSs are formed during volcanic eruptions in the form of lava (mineral CMS),[1] metal casting (alloy CMS),[2] injection moulding (polymer CMS)[3] and in many food related processes such as chocolate crystallization and moulding,[4,5] and butter/margarine crystallization.[6] In the latter case, both the melt phase as well as the crystal phase are composed of triacylglycerols (TAGs), hence the systems are called a TAG CMSs. TAGs, a subclass of lipids, play a major role in the human diet, and TAGs with unsaturated fatty acids have been associated with health beneficial effects.[7] Consequently, recent studies have focused on replacing foods containing TAGs with high saturated fatty acid content with other TAGs containing unsaturated fatty acids or biomacromolecules.[8–11] TAGs with high saturated fatty acid content form CMSs at room temperature and are therefore called fats. They are responsible for the characteristic solid mechanical properties of many foods. Hence, said studies focused on the replacement of the crystal network-forming saturated TAGs with other network forming- or gelling agents such that the solid mechanical properties of the TAG CMSs are matched. However, from an oral processing perspective, not only the solid mechanical properties but also the tribology and shear rheology of the TAG is crucial regarding the organoleptic experience.[12] Recent studies have shown that the volume specific content of saturated fatty acids in TAGs can be successfully reduced by the introduction of gas bubbles thereby forming TAG foams.[13–18] Gas volume fractions up to 0.66 ensure a drastic volume specific reduction in calories and saturated fatty acids while maintaining the melting properties of the TAG crystals.[15] Furthermore, foamed TAGs show similar rheological properties compared to their unfoamed state.[19] Another recent strategy to reduce the intake of saturated fats, sugar and salt is the use of additive manufacturing.[20–22] The spatial arrangement of saturated fats, salt and sugars is designed

[a] *Institute of Food, Nutrition and Health, ETH Zürich, Schmelzbergstrasse 9, 8092 Zürich, Switzerland. E-mail: kim.mishra@hest.ethz.ch; Tel: +41 44 632 97 10*
[b] *Laboratory for Cellulose & Wood Materials, EMPA – Swiss Federal Laboratories for Materials Science and Technology, Überlandstrasse 129, 8600 Dübendorf, Switzerland*
[c] *Electron Microscopy Center, EMPA – Swiss Federal Laboratories for Materials Science and Technology, Überlandstrasse 129, 8600 Dübendorf, Switzerland*

† Electronic supplementary information (ESI) available: Piping and instrumentation diagram of the crystallization and foaming process. Schematic drawing of the UVP-PD measurement set up. XRD spectra of AFM and CB and DSC thermograms of CB directly after crystallization. SEM images of AMF, CB, and PKO crystallized at $\dot{\gamma}_{cryst}$ = 430 s^{-1}. SEM images of AMF, CB, and PKO crystallized at $\dot{\gamma}_{cryst}$ = 1075 s^{-1}. SEM images of AMF, CB, and PKO crystallized at $\dot{\gamma}_{cryst}$ = 2150 s^{-1}. Process settings during DEMF of TAG CMS. The viscosity η as function of shear rate $\dot{\gamma}$ for TAG CMS. See DOI: 10.1039/d1sm01646f

in such a manner that the organoleptic properties of the food are kept constant with less absolute amount of said ingredients. Therefore, to develop new strategies of saturated fatty acid reduction, the rheological properties of TAG CMSs have to be investigated.

CMSs have been characterized as weakly aggregated particle networks, or as suspensions with interpenetrating crystals.[1,23] The percolation threshold Φ_c denotes the crystal volume fraction where the transition from Newtonian to non-Newtonian flow properties takes place.[1,17] Above Φ_c, the CMS shear rheology is adequately described by the Herschel–Bulkley model and the scaling laws for τ_0, n, and K as function of Φ_{SFC} depend on the fractal nature d of the crystal network.[23–28] Recent advances have identified the structural hierarchy governing the formation of networks in TAG CMSs.[29–34] In the following, we adapt the nomenclature of Tang and Marangoni,[34] where crystalline TAGs form lamellae which propagate into domains. The domains stack into single crystallites/platelets, which then aggregate into clusters. The clusters build flocs which form a network. Furthermore, we adapt the concept of Quemada[35] and Windhab[36] describing shear dependent effective volume fractions Φ_{SFC}^{eff} for suspensions.

Despite the knowledge on the morphological structures present in TAG CMSs, little is known on their impact on the bulk shear rheological and foam enhancing properties. Therefore, this work investigates the shear rheological properties of TAG CMSs composed of anhydrous milk fat (AMF), cocoa butter (CB), and palm kernel oil (PKO) by ultrasound velocity profiling – pressure difference (UVP-PD) directly after crystallization by a scraped surface heat exchanger (SSHE). The resulting CMSs are subsequently foamed by dynamically enhanced membrane foaming (DEMF). SSHE rotational speed was varied to gain information on how the crystallization shear rate $\dot{\gamma}_{cryst}$ influences the morphology and structure of the TAG crystals and consequently the rheological properties of the resulting CMS. The produced CMS were investigated by polarized light microscopy (PLM) and scanning electron microscopy (SEM) to probe different levels of structural hierarchy. Differential scanning calorimetry (DSC) and X-ray diffraction (XRD) were applied to determine the polymorphic form of the produced crystals.

2 Materials and methods

2.1 Anhydrous milk fat

AMF was kindly donated by Mibelle AG (Frenkendorf, Switzerland). Countries of origin are Switzerland. The fatty acids were 60% w/w saturated.

2.2 Cocoa butter

CB was kindly donated by Chocolat Frey AG (Buchs, Aargau, Switzerland). Countries of origin are Nigeria, Cameroon, Ivory Coast and Ghana. The fatty acids were 61.5% w/w saturated, 35% w/w monounsaturated and 3.5% w/w polyunsaturated.

2.3 Palm kernel oil

PKO (RSPO-SG) was purchased from Florin AG (Muttenz, Switzerland). The fatty acids were 80% w/w saturated, 17% w/w monounsaturated and 2% w/w polyunsaturated.

2.4 SSHE crystallization

AMF/CB/PKO was fully molten overnight at 40 °C (AMF, PKO) and 45 °C (CB) using a blade stirrer (RW 28W, IKA Werke GmbH, Staufen, Germany) before being crystallized with a scraped surface heat exchanger (SSHE) (Schröder GmbH & Co KG, Lübeck, Germany) as described by Mishra *et al.*[17] The stator diameter $2R_o$ was 60 mm with a length of 400 mm. Using a MS25-HT/P water bath (Julabo Labortechnik GmbH, Seelbach, Germany) with 3.2 kW cooling capacity the double mantled stator was tempered within a temperature range of 5–18 °C. The rotor with two blades had a diameter $2R_i$ of 57 mm and was tempered with a Julabo F32 water bath (Julabo Labortechnik GmbH, Seelbach, Germany) to 23 °C (AMF), 27 °C (PKO), and 32 °C (CB). The rotational speed of the rotor was adjusted by using a V-belt transmission. The crystallization shear rate $\dot{\gamma}_{cryst}$ was calculated by solely considering the velocity field between rotor and stator as described previously:[37–39]

$$\dot{\gamma}_{cryst} = \pi \frac{n_{SSHE}}{15} \frac{R_o^2}{R_o^2 - R_i^2} \quad (1)$$

where n_{SSHE} is the rotational speed, R_o the stator radius and R_i the rotor radius. The investigated $\dot{\gamma}_{cryst}$ were 430, 1075, and 2150 s^{-1} corresponding to 200, 500, and 1000 rpm. An eccentric worm-drive pump (Allweiler GmbH, Radolfzell, Germany) pumped the liquid AMF/CB/PKO from the double mantled stainless steel vessel into the gap between stator and rotor. The piping and instrumentation scheme is displayed in Fig. S1 (ESI†).

2.5 Crystal harvesting and purification for SEM

AMF/CB/PKO CMS was harvested at the SSHE exit. The CMS was diluted with 5 °C MCT (Witarix MCT 60/40, Oleochemicals, Hamburg, Germany) and stirred with a spatula. The resulting diluted CMS was poured onto a suction filter with 4–12 μm retention capacity (MN 615, Macherey-Nagel AG, Oensingen, Switzerland) connected to a 200 mbar vacuum pump. The resulting filter cake was harvested and rinsed with 5 °C ethanol before being filtered a second time with a 1 μm retention glassfibre filter (693, VWR international GmbH, Dietikon, Switzerland). The filtercake was harvested and immediately transferred to −20 °C.

2.6 Polarized light microscopy

Polarized light microscopy (Leica DM6, Leica Microsystems AG, Heerbrugg, Switzerland) was used to investigate crystal morphology. Samples were slightly cooled during imaging by placing an ice container on the stage of the microscope.

2.7 Scanning electron microscopy

About 15 mg of the harvested crystals were diluted with 5 ml ethanol at −20 °C and subsequently vortexed for 30 s. A 50 µl droplet of the crystal in ethanol suspension was dropped onto a freshly cleaved mica disc for 60 s and immediately blown dry with pressurized air without a rinsing step. The mica was then carbon coated with pulse vaporization by means of carbon filament (CCU-010, Safematic GmbH, Zizers, Switzerland). A vacuum below 10^{-5} mbar was applied to deposit carbon films with a layer thickness per pulse of about 0.9 nm amounting to a total layer thickness of 5 nm. The carbon coated micas were then transfered to the SEM (ESEM Quanta FEG650, Thermo Fisher, Waltham, USA) onto a cooled Peltier stage at 1 °C. A vacuum of 0.6 mbar was applied. A fieldemitter (Schottky-emitter) with an electron acceleration voltage of 5 kV was used at a distance of 9–11 mm of the sample surface. A large field detector and concentric back scatter detector were used to capture secondary as well as reflected electrons.

2.8 Crystal volume fraction measurement

Crystal volume fraction Φ_{SFC} was measured by pulsed nuclear magnetic resonance spectroscopy using a 20 MHz (0.47 T) minispec mq20 (Bruker Biospin, Fällanden, Switzerland) in the direct mode. The device was calibrated using paraffin-acrylic standards. Tempered glass tubes with an inner diameter of 1 cm, a wall thickness of 0.06 cm and a height of 18 cm were filled with 3–4 cm of sample and immediately analysed as described previously.[17,37] Triplicates were measured for every porcess setting.

2.9 In-line rheometry by UVP-PD

The UVP-PD measurements were done directly after crystallization as described by Mishra *et al.*[17] Double mantled DN15 pipes held at 23 °C (AMF), 27 °C (PKO), and 32 °C (CB) were used to convey the CMS. The pressure difference was measured in a 3.29 m long pipe section. A diaphragm pressure sensor (CC1020, Labom GmbH, Hude, Germany) with a measurement range of 1.0–1.4 bar absolute pressure was used at the beginning of the pipe segment in order to calculate the pressure difference against atmospheric pressure at the pipe exit. In between the pressure sensor and the end of the pipe segment a custom built polyvinyl chloride cell with inserted ultrasonic transducers was used to record the flow profile. Two 4 MHz transducers (Imasonic SAS, Voray-sur-L'Ognon, France) with an active diameter of 5 mm were placed at 60 and 90 angle with respect to the flow axis in order to determine the velocity profile across the pipe diameter and the speed of sound consecutively. The transducers were preferably operated at 3.75 MHz with a pulse repetition frequency of 750 Hz and 128 repetitions. The signals of the transducers were recorded with the UB-Lab device (Ubertone, Schiltigheim, France). During approximately 60 s a total of six averaged profiles were recorded for one process setting. This procedure was repeated three times for each process setting. Subsequently the profiles were deconvoluted[40, 41, 42] and fitted with the Herschel–Bulkley (HB) model. Fitting the HB model onto the measured velocity profile requires the plug radius R_p, flow index n and consistency factor K as fitting parameters:

$$\nu_{HB}(r) = \begin{cases} \dfrac{n}{n+1} \dfrac{\Delta P^{\frac{1}{n}}}{2L_p K} \left[\left(R - R_p\right)^{1+\frac{1}{n}} - \left(r - R_p\right)^{1+\frac{1}{n}} \right], & \text{if } r \geq R_p \\ \nu_{HB}\left(R_p\right), & \text{if } r < R_p \end{cases} \quad (2)$$

The fitted plug radius R_p is related to the yield stress of the CMS as follows:

$$R_p = \frac{2\tau_0 L_p}{\Delta P} \quad (3)$$

Consequently, the larger R_p and ΔP the higher the yield stress τ_0 of the CMS. A schematic drawing of the measurement track is shown in Fig. S2 (ESI†).

2.10 Differential scanning calorimetry

A differential scanning calorimeter (DSC 3+, Mettler Toledo GmbH, Greifensee, Switzerland) equiped with a FRS 6+ sensor (Mettler Toledo GmbH, Greifensee, Switzerland) was used to investigate the melting behavior of the AMF/CB/PKO CMSs. For each sample, triplicates were measured. Sample weight was 5 ± 0.2 mg for every triplicate. Samples were placed into precooled 40 µl aluminum crucibles (Mettler Toledo GmbH, Greifensee, Switzerland) that weighed 50.49 ± 0.2 mg. Measurements were performed from −30 to +60 °C with a heating rate of +5 °C min^{-1}. Heat flow at a given temperature was evaluated using the STARe-Software (SW 8.1, Mettler Toledo GmbH, Greifensee, Switzerland). In order to avoid further polymorphic changes during sampling and sample storage, a liquid nitrogen (LN_2) bath was used to quench crystallization. Small amounts of the product stream were dropped directly into the LN_2 bath to ensure rapid and uniform cooling. Subsequently, samples were transferred to a dry ice box prior to analysis. Sample preparation was done with precooled instruments.

2.11 X-ray diffraction

An X-ray diffractometer (D8 advanced, Bruker GmbH, Karlsruhe, Germany) was used to characterize the samples in this study. The diffractometer radiation source was Cu-Kα1 with a wavelength of λ = 0.15406 nm and E_{beam} = 40 keV. The diffraction angle 2θ was between 18° and 25° with a step size of 0.02°. Samples were rotated but not tempered during analysis. The total measurement time was 350 s. Sampleholders were precooled in LN_2 before sample deposition. The sampleholders were immediately transferred to a dry ice box and stored therein until analysis.

2.12 Foam formation

A membrane foaming apparatus (Megatron MT-MM 1-52, Kinematica AG, Luzern, Switzerland) was used for the foaming of the CMSs. The dynamically enhanced membrane foaming apparatus consists of two concentric cylinders as previously described by Müller-Fischer *et al.*[43] The static outer cylinder with a radius of 54.5 mm and an axial length of 60 mm consists

of a sintered membrane (Kinematica AG, Luzern, Switzerland) with nominal pore size of 3.5 μm and a porosity of 17%. The inner rotating cylinder with a radius of 44.5 mm generates a defined rheometric shear flow depending on the fluid viscosity and the related Reynolds number (Re) in the 5 mm gap between the outer and inner cylinder thereby detaching the gas bubbles from the membrane surface and dispersing these into the continuous CMS phase. The CMS was axially pumped at 20 kg h^{-1} through the 5 mm annular gap of 60 mm length. Nitrogen gas was injected at 20 l h^{-1} using a floating ball gas flow meter (Q-Flow 80, Vögtlin Instruments GmbH, Muttenz, Switzerland). The inlet pressure of the gas flow meter was set to 7 bar in order to overcome the back-pressure generated by the membrane pores and the static pressure of the continuous CMS phase leading to a calculated gas flow rate of 56 l h^{-1} at atmospheric pressure. Since blow-by was occurring, the rotational speed of the inner cylinder was varied such that the highest possible gas volume fraction Φ_g was incorporated for every investigated Φ_{SFC}. Φ_g analyses were performed at least in triplicates for each process setting.

2.13 Gas volume fraction determination of foamed CMS

The gas volume fraction was determined gravimetrically. The weight of the foamed CMS was measured in 87 ml cups. The cup was slightly overfilled and excess material was wiped off with a spatula. Samples were weighted in triplicates on a Scout Pro SPU6001 scale (Ohaus Corporation, New Jersey, USA), accuracy: ±0.1 g. The gas volume fraction could be determined by:

$$\Phi_g = \frac{m_0 - m_{foam}}{m_0} \quad (4)$$

where m_0 is the weight of 87 ml unfoamed CMS, m_{foam} is the weight of 87 ml foamed CB CMS.

2.14 Statistical analysis

The *x*- and *y*-error bars depicted in Fig. 1, 2 and 6 are calculated standard deviations *s* of the sample using the following equation:

$$s = \sqrt{\frac{1}{N}\sum_{i=1}^{N}(x_i - \bar{x})^2}. \quad (5)$$

where $\bar{x}$ is the mean of the entire sample population, and *N* the number of samples corresponding to analysis repetitions per process setting (≥ 3).

3 Results and discussion

3.1 Rheology of TAG CMS

Molten AMF/CB/PKO was crystallized at different crystallization shear rates $\dot{\gamma}_{cryst}$ and the rheology of the resulting CMS was measured by UVP-PD as function of the crystal volume fraction Φ_{SFC}. XRD and DSC measurements identified β' as the predominant crystal polymorph in the AMF and PKO[17] CMS and β_v as the predominant crystal polymorph in the CB CMS for all crystallization shear rates as shown in Fig. S3 (ESI†). For CB

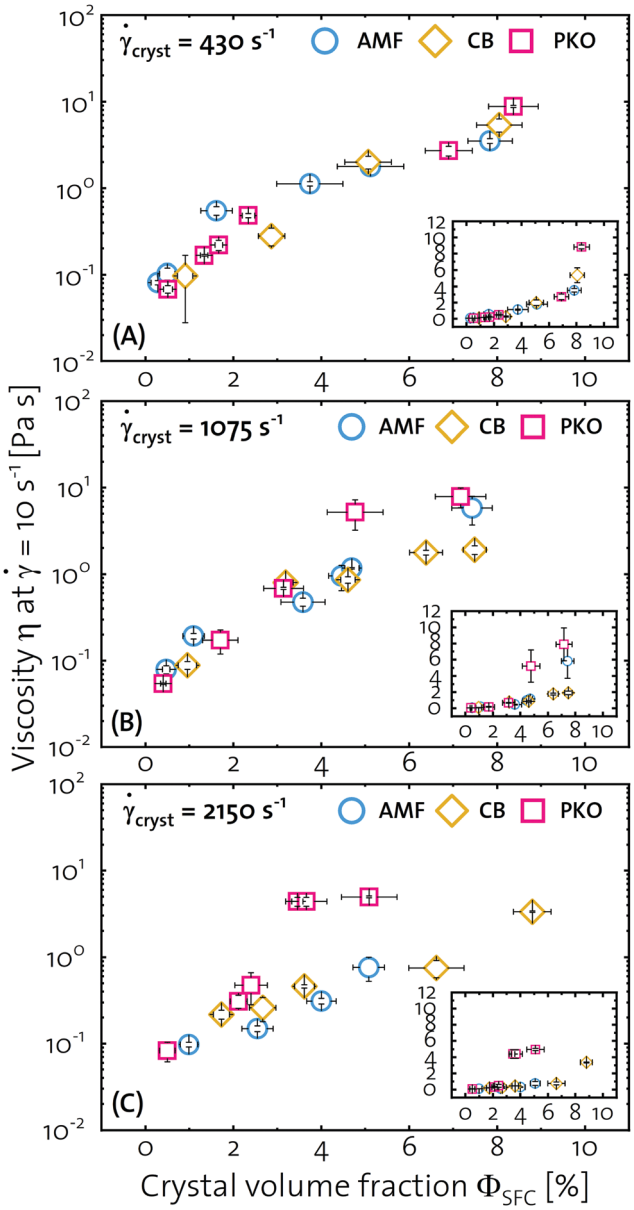

Fig. 1 The viscosity η at $\dot{\gamma}$ = 10 s^{-1} as function of the crystal volume fraction Φ_{SFC} for CMSs consisting of AMF/CB/PKO crystallized at $\dot{\gamma}_{cryst}$ = (A) 430, (B) 1075, and (C) 2150 s^{-1}. The data of CB CMS crystallized at 2150 s^{-1} was reproduced from Mishra *et al.*[19] The inserts in the graphs depict the same data with a linear *y*-axis.

CMS crystallized at $\dot{\gamma}_{cryst}$ = 430 s^{-1}, also residuals of polymorphic form II are present. Fig. 1 shows the measured shear viscosity η at $\dot{\gamma}$ = 10 s^{-1} for AMF/CB/PKO CMSs produced at $\dot{\gamma}_{cryst}$ = (A) 430, (B) 1075 and (C) 2150 s^{-1}. All investigated CMSs show very similar values of η as function of Φ_{SFC} for $\dot{\gamma}_{cryst}$ = 430 s^{-1} (Fig. 1(A)), which is apparent by the collapse of the data on the same line. Fig. 1(B) shows that the data diverges above $\Phi_{SFC} \approx 4\%$ for AMF/CB/PKO crystallized at $\dot{\gamma}_{cryst}$ = 1075 s^{-1}. PKO and AMF show increased η values compared to CB above $\Phi_{SFC} \approx 4\%$. Fig. 1(C), where the CMSs were crystallized at $\dot{\gamma}_{cryst}$ = 2150 s^{-1}, shows a divergence of the data above $\Phi_{SFC} \approx 3\%$. PKO shows higher η than AMF and CB. AMF and CB show

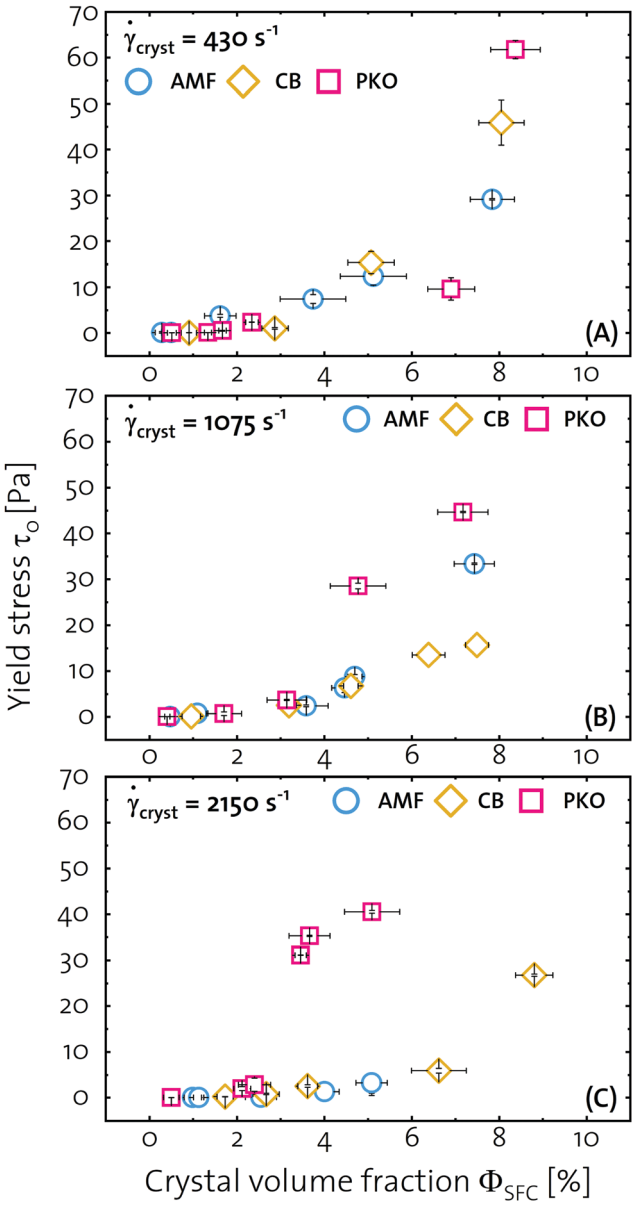

Fig. 2 The yield stress τ_0 as function of the crystal volume fraction Φ_{SFC} for CMSs consisting of AMF/CB/PKO crystallized at $\dot{\gamma}_{cryst}$ = (A) 430, (B) 1075, and (C) 2150 s^{-1}. The data of PKO CMS was reproduced from Mishra *et al.*[17]

very similar η. Overall, a non-linear dependency between η and Φ_{SFC} is apparent for all $\dot{\gamma}_{cryst}$ as predicted by Saar *et al.*[1] However, at low Φ_{SFC} a linear regime is observed as shown by the inserts in Fig. 1. For PKO, the critical crystal concentration Φ_c for the onset of a non-linearity is shifted towards smaller Φ_{SFC} with increasing $\dot{\gamma}_{cryst}$, whereas for AMF and CB the opposite is the case. Furthermore, PKO viscosity for a given Φ_{SFC} is increasing with increasing $\dot{\gamma}_{cryst}$, whereas AMF and CB viscosities for a given Φ_{SFC} are slightly decreasing with increasing $\dot{\gamma}_{cryst}$. The different dependencies of η as function of Φ_{SFC} for increasing $\dot{\gamma}_{cryst}$ are a result of the crystallite aspect ratio $a_{crystallite}$ and the aggregation of those crystallites into clusters and ultimatively into flocs. According to Saar *et al.*,[1] the onset of the yield stress τ_0 as function of Φ_{SFC} is connected to $a_{cluster}$ and $a_{crystallite}$. Marangoni and Rogers[23] relate the crystallite and crystallite cluster radius with the scaling of τ_0 as function of Φ_{SFC}. Therefore, τ_0 was derived from the UVP-PD data.

Fig. 2 shows the yield stress τ_0 as function of the crystal volume fraction Φ_{SFC} for CMSs crystallized at various crystallization shear rates $\dot{\gamma}_{cryst}$. Fig. 2(A) shows the data obtained for CMSs crystallized at $\dot{\gamma}_{cryst}$ = 430 s^{-1}. The slope of the $\tau_0 = f(\Phi_{SFC})$-curve is very similar for all CMSs, which is apparent by the collapse of the data on the same line. Moving to higher $\dot{\gamma}_{cryst}$ of 1075 s^{-1}, the data diverges at $\Phi_{SFC} \approx 4\%$. The slope of the PKO $\tau_0 = f(\Phi_{SFC})$-curve is higher than for AMF and CB. A second divergence occurs at $\Phi_{SFC} \approx 5\%$ where AMF shows higher τ_0 than CB. At $\dot{\gamma}_{cryst}$ = 2150 s^{-1}, the data diverges below $\Phi_{SFC} \approx 2\%$ since the slope of the PKO $\tau_0 = f(\Phi_{SFC})$-curve is becoming increasingly steep. AMF and CB show flattened $\tau_0 = f(\Phi_{SFC})$-curve slopes. Overall, for PKO the $\tau_0 = f(\Phi_{SFC})$-curve becomes increasingly steep with increasing $\dot{\gamma}_{cryst}$, whereas for AMF and CB the $\tau_0 = f(\Phi_{SFC})$-curve flatten with increasing $\dot{\gamma}_{cryst}$. From the data presented in Fig. 2, we deduce that for PKO the τ_0 at a given Φ_{SFC} increases as function of $\dot{\gamma}_{cryst}$, whereas for AMF and CB the opposite is the case. The critical crystal volume fraction Φ_c for the onset of τ_0 is decreased for PKO and increased for AMF and CB with increasing $\dot{\gamma}_{cryst}$.

Summarizing the findings from Fig. 1 and 2 we conclude that at $\dot{\gamma}_{cryst}$ = 430 s^{-1}, similar η and τ_0 values are reached for AMF, CB, and PKO CMSs leading to the collapse of the data on the same line over the entire investigated Φ_{SFC}-range. The Φ_{SFC}-range where a linear relationship between η and Φ_{SFC} is apparent coincides with the absence of τ_0 indicating that Φ_c has not been reached. Above Φ_c, the non-linear relationship of η and τ_0 with Φ_{SFC} are a result of crystal percolation and network formation. From the theories developed by Saar *et al.*[1] and Marangoni and Rogers[23] the decreased Φ_c for PKO and increased slope of η and τ_0 as function of Φ_{SFC} with increasing $\dot{\gamma}_{cryst}$ implies that smaller crystallites and crystallite clusters with increased aspect ratios are formed. For AMF and CB the increased Φ_c and decreased slope of η and τ_0 with increasing $\dot{\gamma}_{cryst}$ implies that larger crystallites and crystallite clusters with decreased aspect ratios are formed. In order to confirm this implication, scanning electron microscopy (SEM) and polarized light microscopy (PLM) were performed.

3.2 Crystal microstructure of TAG CMS

Fig. 3–5 show SEM and PLM images of AMF-, CB-, and PKO CMSs after crystallization at $\dot{\gamma}_{cryst}$ = 430, 1075 and 2150 s^{-1}. Additional SEM images are displayed in Fig. S4–S6 (ESI†). Using the nomenclature for crystal micro- and nano-structures proposed by Tang and Marangoni,[34] we are able to distinguish between crystallites, crystallite clusters, and crystal flocs.

Fig. 3(A–C) show the morphology of AMF crystallite clusters as function of $\dot{\gamma}_{cryst}$. At all $\dot{\gamma}_{cryst}$, spherical crystallite clusters with furrowed surfaces are apparent. The furrowed surface indicates that the imaged objects are indeed crystallite clusters composed of single crystallites. The crystallite cluster size is gradually decreasing with increasing $\dot{\gamma}_{cryst}$. Judging from the

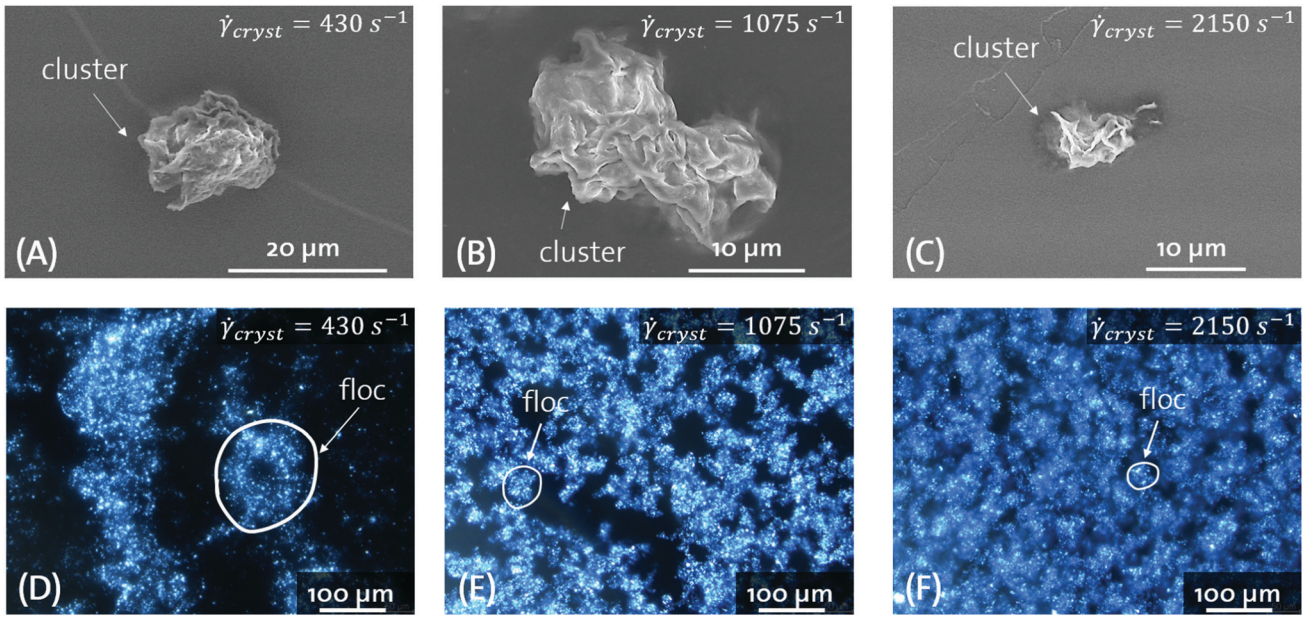

Fig. 3 SEM (A–C) and PLM (D–F) images of AMF crystallized at $\dot{\gamma}_{cryst}$ = (A and D) 430, (B and E) 1075, and (C and F) 2150 s^{-1}. Additional SEM images are displayed in Fig. S4 (ESI†).

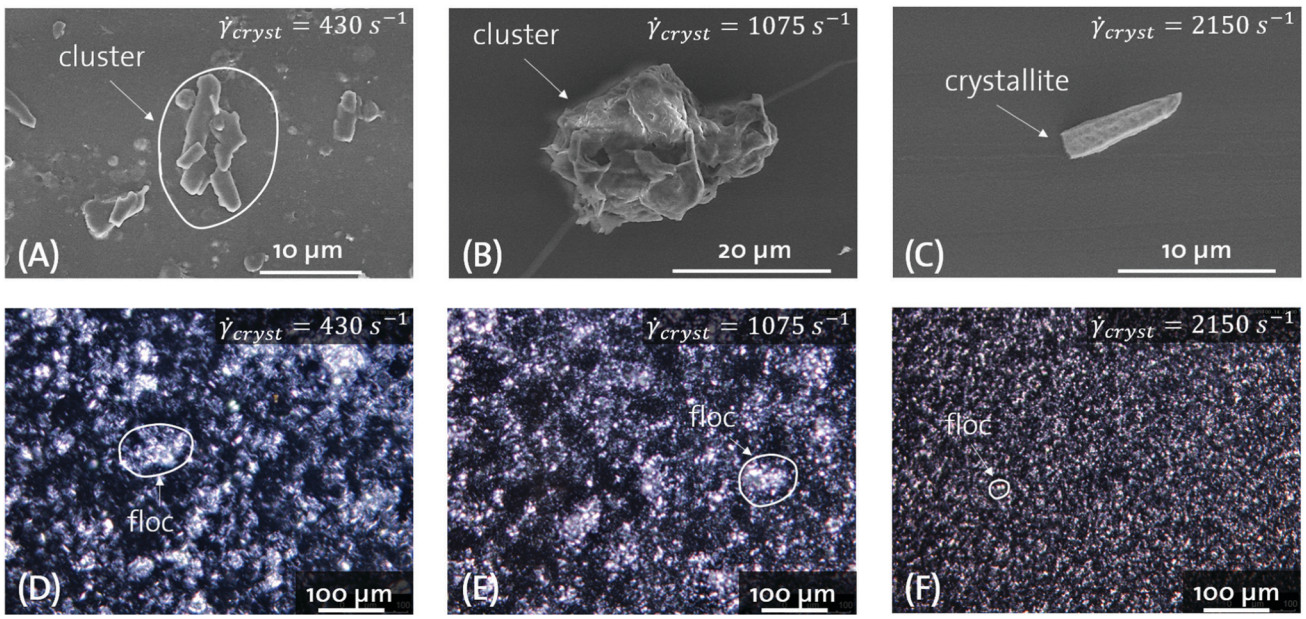

Fig. 4 SEM (A–C) and PLM (D–F) images of CB crystallized at $\dot{\gamma}_{cryst}$ = (A and D) 430, (B and E) 1075, and (C and F) 2150 s^{-1}. Additional SEM images are displayed in Fig. S5 (ESI†).

width and the length of the crystallite clusters, no significant change in $a_{cluster}$ is observed. Fig. 3(D–F) shows the aggregation of crystallite clusters into crystal flocs and the aggregation of the flocs into a network. At $\dot{\gamma}_{cryst}$ = 430 s^{-1}, the crystal floc diameter is in the range of ≈ 100 µm. With increasing $\dot{\gamma}_{cryst}$, the floc diameter decreases to ≈ 30–50 µm at $\dot{\gamma}_{cryst}$ = 1075 and 2150 s^{-1}. From Fig. 3, we conclude that for AMF $a_{cluster}$ is not changing with increasing $\dot{\gamma}_{cryst}$. Only the crystallite cluster and floc diameter decrease with increasing $\dot{\gamma}_{cryst}$.

Fig. 4(A–C) shows the morphology of CB crystallite clusters as function of $\dot{\gamma}_{cryst}$. At $\dot{\gamma}_{cryst}$ = 430 s^{-1}, platelet-like single crystallites form small and loosely packed crystallite clusters. At $\dot{\gamma}_{cryst}$ = 1075 s^{-1}, platelet-like single crystallites form larger and denser packed clusters. Moving to highest crystallization shear rates of $\dot{\gamma}_{cryst}$ = 2150 s^{-1}, platelet-like single crystallites are observed. Fig. 4(D–F) show PLM images of the CB CMS directly after crystallization. At $\dot{\gamma}_{cryst}$ = 430 s^{-1}, the aggregation of crystallite clusters into flocs with a diameter of 40–80 µm is

apparent. The flocs are composed of crystallite clusters with $a_{cluster} > 1$. At $\dot{\gamma}_{cryst} = 1075\ s^{-1}$, the crystal flocs are less densely packed compared to $\dot{\gamma}_{cryst} = 430\ s^{-1}$ but show similar diameters of 40–80 μm. The crystallite clusters building the flocs show spherical shapes. At $\dot{\gamma}_{cryst} = 2150\ s^{-1}$, the crystal flocs are deaggregated and suspended crystallite clusters with a diameter <20 μm are visible.

Fig. 5(A–C) shows the morphology of PKO crystallite clusters and crystallites as function of $\dot{\gamma}_{cryst}$. At $\dot{\gamma}_{cryst} = 430\ s^{-1}$, platelet-like single crystallites with $a_{crystallite} > 1$ are imaged. They form densely packed clusters with a diameter of ≈5–8 μm and a cluster aspect ratio $a_{cluster} \approx 1$. At $\dot{\gamma}_{cryst} = 1075\ s^{-1}$, platelet-like single crystallites with $a_{crystallite} > 1$ are imaged. The crystallite length and width is greater compared to the crystals produced at $\dot{\gamma}_{cryst} = 430\ s^{-1}$. Single crystallites as well as crystallite clusters are present as depicted by Fig. S6 (ESI†) where crystallite clusters with $a_{cluster} \approx 1$ and a diameter between 30 and 40 μm are shown. Moving to highest crystallization shear rates of $\dot{\gamma}_{cryst} = 2150\ s^{-1}$, needle-like single crystallites are observed. Assuming prolate crystallites, the $a_{crystallite}$ is $\gg 1$. Fig. 5(D–F) show PLM images of the PKO CMS directly after crystallization. At $\dot{\gamma}_{cryst} = 430\ s^{-1}$, dense crystal flocs with a diameter of ≈50–80 μm are imaged. The individual crystallite clusters are not visible. At $\dot{\gamma}_{cryst} = 1075\ s^{-1}$, the crystal floc size is decreased to 30–50 μm. They are composed of needle-like crystallite clusters which are loosely connected. At $\dot{\gamma}_{cryst} = 2150\ s^{-1}$, the crystal floc size is further decreased to 20–40 μm. The flocs are composed of needle-like crystallite clusters. Single crystallites are visible.

The results of Fig. 3–5 contradict the rheological models. Larger crystallites and crystallite clusters having reduced aspect ratios are predicted from the decreased $\tau_0 = f(\Phi_{SFC})$-slopes and decreased Φ_c observed for AMF and PKO CMS at high $\dot{\gamma}_{cryst}$.[1,23]

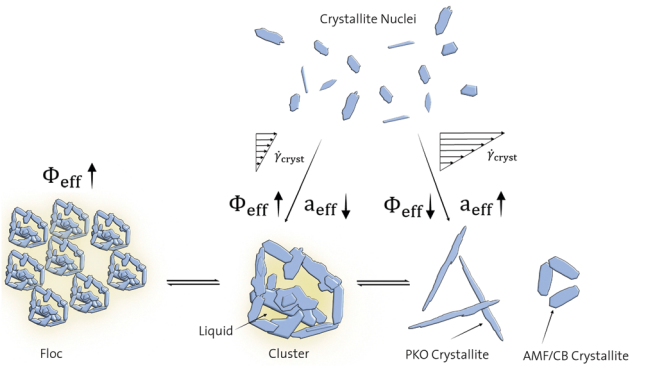

Fig. 6 Schematic illustration of crystallite nucleus growth and aggregation into clusters and flocs at different crystallization shear rates $\dot{\gamma}_{cryst}$ for AMF-, CB-, and PKO CMS.

Therefore, a different mechanism as illustrated in Fig. 6 is proposed to connect the observed microstructures with the rheological findings: At high $\dot{\gamma}_{cryst}$, the crystallite nuclei are growing as isolated crystallites in the shear flow field, which increases the effective aspect ratio a_{eff} of the suspended crystalline particles and decreases the effective crystal volume fraction Φ_{SFC}^{eff}. At low $\dot{\gamma}_{cryst}$, the direct aggregation of the crystallite nuclei into crystallite clusters leads to the entrapment of continuous phase thereby increasing Φ_{SFC}^{eff} but also decreasing a_{eff}. At high $\dot{\gamma}_{cryst}$, the isolated crystallites eventually aggregate into crystallite clusters and *vice versa* depending on the ratio between acting shear stresses τ and cluster adhesion strength, thereby forming a dynamic equilibrium. Aggregation of crystallite clusters into flocs occurs as a result of the same mechanism. However, $a_{cluster}$ and a_{floc} remain constant, while Φ_{SFC}^{eff} increases from cluster to floc. The molecular origin determining the

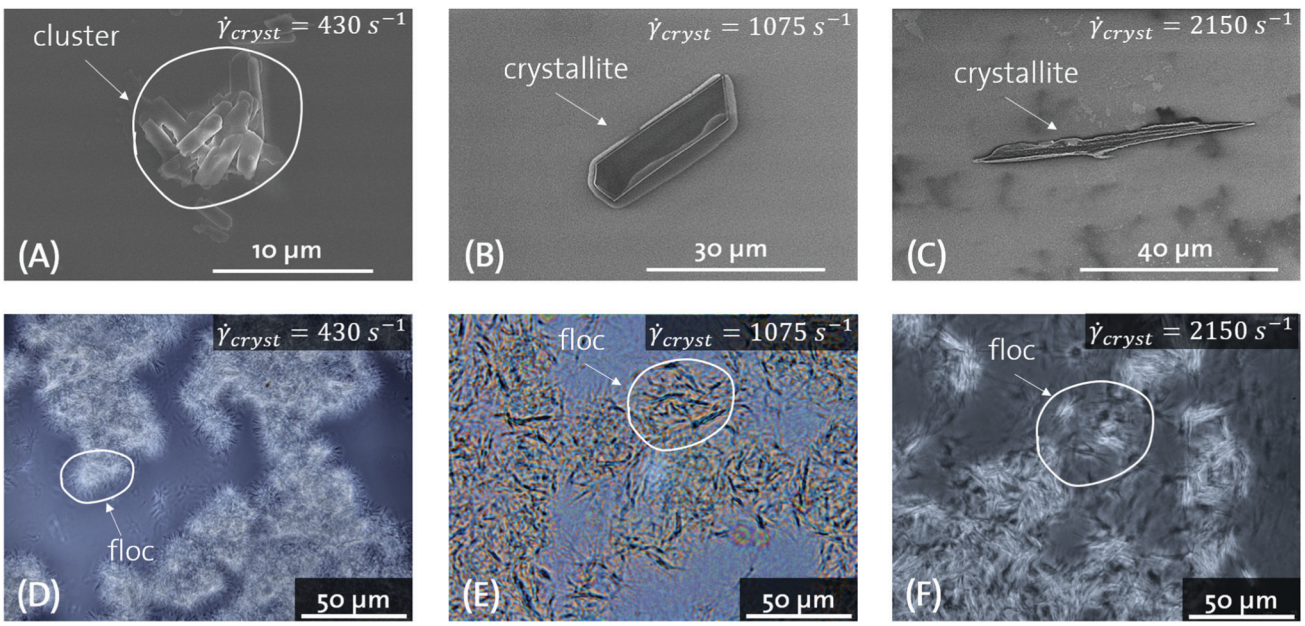

Fig. 5 SEM (A–C) and PLM (D–F) images of PKO crystallized at $\dot{\gamma}_{cryst}$ = (A and D) 430, (B and E) 1075, and (C and F) 2150 s^{-1}. Additional SEM images are displayed in Fig. S6 (ESI†).

crystallite cluster and floc strength is related to the TAG composition. PKO shows a high amount of trilaurin and other TAGs composed of completely saturated fatty acids, whereas AMF and CB contain high amount of monounsaturated TAGs.[44–46] Previous studies have shown that small amounts of monounsaturated TAGs lead to the formation of rough crystallite surfaces, whereas completely saturated TAGs form smooth surfaces.[47] Hence, the saturated TAGs present in PKO form crystallites with smooth surfaces thereby reducing crystallite cluster and floc adhesion strength. As a consequence, the dynamic equilibrium is shifted towards the isolated crystallites leading to their prolonged exposure in the shear gradient. The shear gradient induces directed growth parallel to the velocity vectors thereby minimizing drag and increasing $a_{crystallite}$. On the contrary, the relatively high amount of unsaturated TAGs present in AMF and PKO form crystallites with rough surfaces thereby increasing crystallite cluster and floc adhesion strength and shifting the equilibrium towards the crystallite clusters and flocs. The increased aggregation of crystallites into clusters reduces their exposure to the shear flow field thereby reducing $a_{crystallite}$. At $\dot{\gamma}_{cryst}$ = 430 s^{-1}, AMF/CB/PKO crystallites are mainly present in the form of clusters and flocs with similar sizes and aspect ratios leading to almost identical rheological behvaior of the corresponding CMSs. At $\dot{\gamma}_{cryst}$ = 1075 s^{-1} and 2150 s^{-1}, the clusters and flocs are partially deaggregated into single crystallites. In the case of AMF and CB, the released liquid continuous phase reducing Φ_{eff} is dominating the rheological behavior due to the low $a_{crystallite}$. In the case of PKO, the increased $a_{crystallite}$ dominates over the reduced Φ_{eff} regarding the rheological behavior.

3.3 Foamability of TAG CMS

Reducing the volume specific content of saturated fatty acids of AMF-, CB-, and PKO CMS can be achieved by introducing gas bubbles thereby forming a foam. It remains unclear whether long needle-like crystallites or spherical crystallite clusters favor foam formation.[15–17] Several observations exist: Mishima *et al.*[15] states that small β crystals are promoting foam formation, Binks and Marinopoulos[16] are indicating a Φ_{SFC} of 10–30%, and Mishra *et al.*[17] relates gas bubble diameter to the Bingham number acting during dispersion. Therefore, the different CMS were foamed by using the DEMF process to test which crystal microstructure yields the highest foamability.

Fig. 7 shows the maximally achievable gas volume fraction of (A) AMF, (B) CB, and (C) PKO CMSs foamed with the DEMF continuous process directly after crystallization. The piping and instrumentation scheme is displayed in Fig. S1 (ESI†). Table S1 (ESI†) lists the processing settings and the average acting shear rates in the annular gap $\dot{\gamma}_{gap}$ during foam formation. Fig. S7 (ESI†) shows the viscosity as function of shear rate $\dot{\gamma}$ for the continuous phase TAG CMSs. Comparing Table S1 and Fig. S7 (ESI†), it becomes apparent that the $\dot{\gamma}$-range determined by UVP-PD is lower than the acting $\dot{\gamma}_{gap}$. Furthermore, with increasing $\dot{\gamma}$ the differences between the varying Φ_{SFC} become smaller as a result of shear-thinning. However, due to the large annular gap width of 5 mm, the shear rate acting at the membrane surface is considerably lower compared to the $\dot{\gamma}_{gap}$. Hence, the qualitative differences between the TAG CMS viscosities as function of TAG and Φ_{SFC} deduced from Fig. 1 are applicable during the foam formation process. For $\dot{\gamma}_{cryst}$ = 430 s^{-1}, AMF and CB CMSs show increasing gas volume fraction Φ_g with increasing Φ_{SFC}. The highest Φ_g reached for AMF CMS is 0.41 ± 0.05 at Φ_{SFC} = 7.2 ± 0.5% and for CB CMS 0.55 ± 0.02 at Φ_{SFC} = 10.3 ± 0.6% which is similar to the values proposed by Binks and Marinopoulos[16] and Mishima *et al.*[15] The PKO CMS shows no monotonic increase in Φ_g as function of Φ_{SFC}. Φ_g peaks at Φ_{SFC} = 2.2 ± 0.6% with a value of 0.36 ± 0.02 before decreasing to lower Φ_g with increasing Φ_{SFC}. At $\dot{\gamma}_{cryst}$ = 2150 s^{-1}, AMF and CB CMSs show poor foamability.

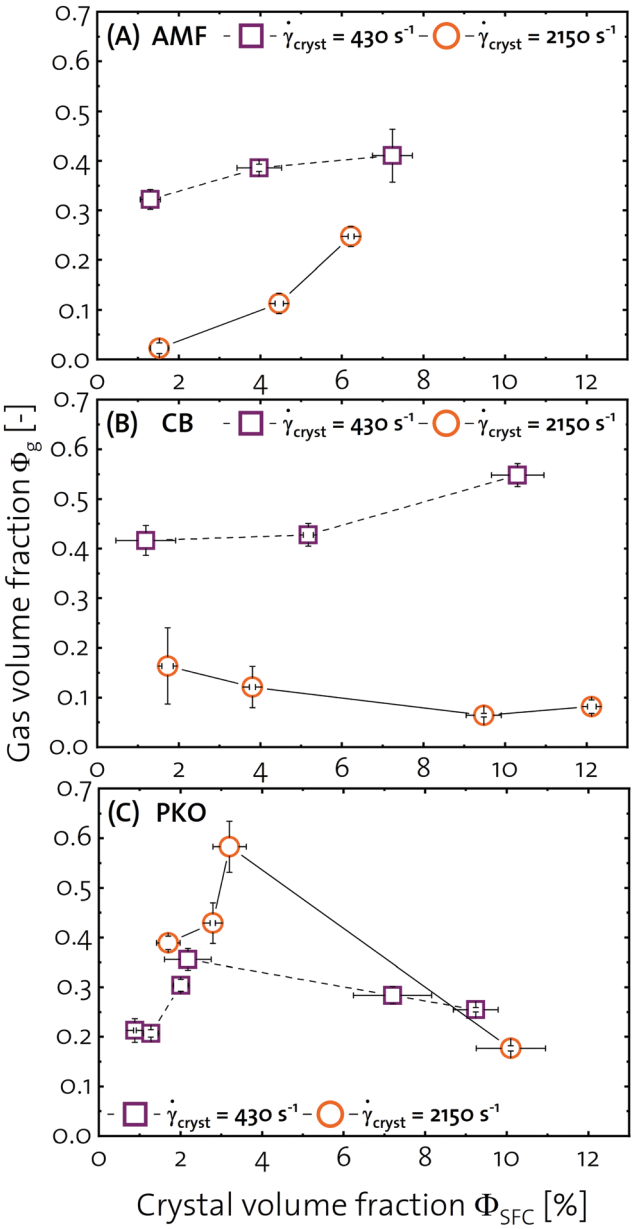

Fig. 7 The maximally achievable gas volume fraction Φ_g as function of crystal volume fraction Φ_{SFC} for AMF/CB/PKO CMSs crystallized at $\dot{\gamma}_{cryst}$ = 430 s^{-1} and 2150 s^{-1}.

AMF CMS shows increasing Φ_g with Φ_{SFC} and CB CMS decreasing Φ_g with Φ_{SFC}. PKO CMS shows again a peak-like dependency of Φ_g with Φ_{SFC}, which has been observed as well by Binks and Marinopoulos[16] for other TAG CMS. Φ_g up to 0.58 ± 0.05 at Φ_{SFC} = 3.2 ± 0.4% are reached. Following the journey of a gas bubble detaching from the membrane into the annular gap, the subsequent residence time of the bubble in the gap and ultimately the exit of the bubble from the annular gap into the outlet DN15 pipe, the influence of TAG CMS η and τ_0 on gas bubble stabilization is deduced: In the annular gap, the centrifugal force drives gas bubbles towards the rotating cylinder. The resulting bubble velocity towards the inner rotating cylinder is inversely proportional to the TAG CMS continuous phase η. Hence, low TAG CMS η promotes demixing of the continuous phase and the dispersed gas bubbles leading to blow-by. High TAG CMS η on the other hand reduces bubble dispersion into the annular gap. High TAG CMS τ_0 leads to the formation of unyielded CMS close to the membrane surface thereby reducing the demixing effects caused by the centrifugal forces. During the residence time in the annular gap, increased TAG CMS η induces higher shear stresses acting on the gas bubbles which leads to further break-up. However, with increasing η, the characteristic time scale for gas bubble stabilization is increased in case of Pickering stabilization (diffusion limited) but not in case of network induced immobilization. This increased stabilization time leads to higher coalescence rates after gas bubble break-up. Once the foam is conveyed in the outlet pipe, the yield stress τ_0 magnitude determines the plug radius R_p. Gas bubbles residing at radial positions $r \leq R_p$ are immobilized and can not coalesce or demix. Consequently, increased τ_0 leads to higher gas bubble stabilization in the outlet pipe.

The results presented in Fig. 7 show that for AMF and CB CMSs, the decrease in η and τ_0 with increasing $\dot{\gamma}_{cryst}$ results in lower Φ_g. The decrease in Φ_g with increasing $\dot{\gamma}_{cryst}$ and the associated reduction in η and τ_0 points towards gas bubble stabilization by network immobilization as previously described by Mishra *et al.*[17] The small crystallite clusters and isolated crystallites formed at high $\dot{\gamma}_{cryst}$ are not stabilizing the gas bubbles fast enough leading to a centrifugal demixing in the annular gap causing blow-by, thereby reducing Φ_g. The low stabilization potential of the small crystallite clusters and isolated crystallites originates from their surface roughness which reduces the contact area with the gas bubble interface.[48] For PKO CMS, the peak value of Φ_g as function of Φ_{SFC} is close to the percolation threshold Φ_c. This shows that a continuous network is required to stabilize gas bubbles indicating a network immobilization mechanism. The formation of needle-like crystallites at high $\dot{\gamma}_{cryst}$ leads to the increase in both η and τ_0 as well as Φ_g confirming the network immobilization mechanism. However, the peak Φ_g is followed by a subsequent decrease as function of Φ_{SFC} indicating that the increased η and τ_0 are reducing gas bubble stabilization. Hence, a Pickering stabilization is most likely to occur as long as the CMS η and τ_0 are low enough and the crystallites can diffuse to the gas bubble interface. However, the peaking of Φ_g as function of Φ_{SFC} is apparent at both $\dot{\gamma}_{cryst}$, which contradicts the morphological findings that at low $\dot{\gamma}_{cryst}$ mainly crystallite clusters are present. This implies that also crystallite clusters act as Pickering particles. The foam stabilization potential of PKO crystallites and crystallite clusters originates from their smooth surface which increases contact area with the gas bubble interface.

The findings presented above extend the conclusions drawn by previous studies on the foamability of TAG CMS where it is hypothesized that gas bubble stabilization occurs by a Pickering mechanism of TAG crystallites.[15,16,49] Our findings show that there is an interplay between the bulk rheological properties (η, τ_0) and crystal floc, crystallite cluster and crystallite morphology which determines TAG CMS foamability. Depending on TAG composition, the CMS bulk rheological properties as well as the Pickering potential of crystallites and crystallite clusters is altered. CMS containing TAGs with high unsaturated fatty acid content incorporate gas bubbles by network immobilization. CMS containing TAGs with high saturated fatty acid content stabilize gas bubbles by a combination of Pickering and network immobilization.

4 Conclusion

We show that the rheology of lipid CMSs consisting of TAGs from either AMF, CB and PKO is governed by both, the single crystallite size and morphology as well as their aggregation into crystallite clusters and flocs. The TAG composition dependent surface properties of the crystallites determine the aggregation rate into crystallite clusters. AMF and CB containing more TAGs with unsaturated fatty acids form crystallites with rough surfaces, whereas PKO containing more TAGs with saturated fatty acids forms crystallites with smooth surfaces. Crystallites with rough surfaces aggregate into crystallite clusters faster. Such clusters immobilize liquid continuous phase and are therefore increasing the effective crystal volume fraction. Crystallites with smooth surfaces are less prone to aggregate leading to prolonged exposure in the shear gradient and hence the formation of high aspect ratio crystallites. At low crystallization shear rates, the rapid aggregation of the crystallites into spherical clusters leads to similar rheological behavior for AMF, CB and PKO CMS. At high crystallization shear rates, less crystallite clusters are formed and isolated crystallites are present. AMF and CB CMS show lower η and τ_0 values due to the dominating effect of reduced effective volume fraction, whereas PKO CMS shows increased η and τ_0 due to the dominating effect of increased effective aspect ratio.

The correlation of TAG CMS rheology and microstructure with its foamability reveals different stabilization mechanisms. For AMF and CB CMS, gas bubbles are mainly stabilized by the immobilization into the continuous floc network. For PKO CMS a combined network immobilization and single crystallite/crystallite cluster adsorption by a Pickering mechanism is responsible for gas bubble stabilization.

The new techniques and methodologies presented in this work allow to relate the rheology of TAG CMS to the morphology and

size of their crystallites, crystallite clusters and crystal flocs and shows how to use shear during crystallization to taylor CMS rheology. This work contributes to the understanding of the interplay between CMS microstructure, rheology, and foamability which opens new possibilities to reduce the energy density and volume specific content of saturated fatty acids in lipids. The detailed understanding of liquid continuous phase immobilization gives rise to new strategies for fat production from novel lipid sources such as microorganisms.

Author contributions

Kim Mishra – conceptualization, project administration, investigation, methodology, supervision, software, validation, visualization, writing. Fabian Kämpf – data curation, formal analysis, investigation. Silas Ehrengruber – data curation, formal analysis, investigation. Julia Merkel – data curation, formal analysis, investigation. Nico Kummer – conceptualization, data curation, investigation, methodology. Robin Pauer – investigation, methodology. Peter Fischer – conceptualization, data curation, validation. Erich J. Windhab – conceptualization, data curation, validation, funding acquisition.

Conflicts of interest

There are no conflicts to declare.

Acknowledgements

The authors thank the Swiss National Science Foundation and Innosuisse for funding of the Bridge project 20B2-1-180971/1.

Notes and references

1 M. O. Saar, M. Manga, K. V. Cashman and S. Fremouw, *Earth Planet. Sci. Lett.*, 2001, **187**, 367–379.
2 P. Joly and R. Mehrabian, *J. Mater. Sci.*, 1976, **11**, 1393–1418.
3 S. S. Katti and M. Schultz, *Polym. Eng. Sci.*, 1982, **22**, 1001–1017.
4 L. Grob, K. Papadea, P. Braun and E. J. Windhab, *J. Food Eng.*, 2021, **292**, 110322.
5 L. Grob, K. Papadea, P. Braun and E. J. Windhab, *Innovative Food Sci. Emerging Technol.*, 2021, **68**, 102629.
6 A. Wright, M. Scanlon, R. Hartel and A. Marangoni, *J. Food Sci.*, 2001, **66**, 1056–1071.
7 E. Sokoła-Wysoczańska, T. Wysoczański, J. Wagner, K. Czyż, R. Bodkowski, S. Lochyński and B. Patkowska-Sokoła, *Nutrients*, 2018, **10**, 1561.
8 C. Woern, A. G. Marangoni, J. Weiss and S. Barbut, *Food Res. Int.*, 2021, **147**, 110431.
9 M. López-Pedrouso, J. M. Lorenzo, B. Gullón, P. C. B. Campagnol and D. Franco, *Curr. Opin. Food Sci.*, 2021, **40**, 40–45.
10 Y. Kumar, *Food Rev. Int.*, 2021, **37**, 296–312.
11 A. R. Patel, R. A. Nicholson and A. G. Marangoni, *Curr. Opin. Food Sci.*, 2020, **33**, 61–68.
12 B. J. Le Révérend, I. T. Norton, P. W. Cox and F. Spyropoulos, *Curr. Opin. Colloid Interface Sci.*, 2010, **15**, 84–89.
13 A.-L. Fameau, S. Lam, A. Arnould, C. Gaillard, O. D. Velev and A. Saint-Jalmes, *Langmuir*, 2015, **31**, 13501–13510.
14 M. Brun, M. Delample, E. Harte, S. Lecomte and F. Leal-Calderon, *Food Res. Int.*, 2015, **67**, 366–375.
15 S. Mishima, A. Suzuki, K. Sato and S. Ueno, *J. Am. Oil Chem. Soc.*, 2016, **93**, 1453–1466.
16 B. P. Binks and I. Marinopoulos, *Food Res. Int.*, 2017, **95**, 28–37.
17 K. Mishra, D. Dufour and E. J. Windhab, *Cryst. Growth Des.*, 2020, **20**, 1292–1301.
18 K. Mishra, J. Bergfreund, P. Bertsch, P. Fischer and E. J. Windhab, *Langmuir*, 2020, **36**, 7566–7572.
19 K. Mishra, L. Grob, L. Kohler, S. Zimmermann, S. Gstöhl, P. Fischer and E. J. Windhab, *J. Rheol.*, 2021, **65**, 1155–1168.
20 S. Mantihal, S. Prakash, F. C. Godoi and B. Bhandari, *Food Res. Int.*, 2019, **119**, 161–169.
21 S. Prakash, B. R. Bhandari, F. C. Godoi and M. Zhang, *Fundamentals of 3D food printing and applications*, Elsevier, 2019, pp. 373–381.
22 P. Rando and M. Ramaioli, *J. Food Eng.*, 2021, **294**, 110415.
23 A. G. Marangoni and M. A. Rogers, *Appl. Phys. Lett.*, 2003, **82**, 3239–3241.
24 K. Mishra, L. Kohler, N. Kummer, S. Zimmermann, S. Ehrengruber, F. Kämpf, D. Dufour, G. Nyström, P. Fischer and E. J. Windhab, *J. Food Eng.*, 2021, **305**, 110598.
25 T. S. Awad, M. A. Rogers and A. G. Marangoni, *J. Phys. Chem. B*, 2004, **108**, 171–179.
26 S. S. Narine and A. G. Marangoni, *Phys. Rev. E: Stat. Phys., Plasmas, Fluids, Relat. Interdiscip. Top.*, 1999, **59**, 1908–1920.
27 W.-H. W. Y. Shih, S.-I. Kim, J. Liu and I. A. Aksay, *Phys. Rev. A: At., Mol., Opt. Phys.*, 1990, **42**, 4772–4779.
28 R. Vreeker, L. Hoekstra, D. den Boer and W. Agterof, *Colloids Surf.*, 1992, **65**, 185–189.
29 A. G. Marangoni, J. P. Van Duynhoven, N. C. Acevedo, R. A. Nicholson and A. R. Patel, *Soft Matter*, 2020, **16**, 289–306.
30 P. R. Ramel, E. D. Co, N. C. Acevedo and A. G. Marangoni, *Prog. Lipid Res.*, 2016, **64**, 231–242.
31 F. Peyronel, D. A. Pink and A. G. Marangoni, *Curr. Opin. Colloid Interface Sci.*, 2014, **19**, 459–470.
32 N. C. Acevedo, F. Peyronel and A. G. Marangoni, *Curr. Opin. Colloid Interface Sci.*, 2011, **16**, 374–383.
33 N. C. Acevedo and A. G. Marangoni, *Cryst. Growth Des.*, 2010, **10**, 3327–3333.
34 D. Tang and A. G. Marangoni, *Adv. Colloid Interface Sci.*, 2006, **128**, 257–265.
35 D. Quemada, *Eur. Phys. J.: Appl. Phys.*, 1998, **1**, 119–127.
36 E. J. Windhab, *Appl. Rheol.*, 2000, **10**, 134–144.
37 B. Breitschuh and E. J. Windhab, *J. Am. Oil Chem. Soc.*, 1996, **73**, 1603–1610.
38 E. Dumont, F. Fayolle and J. Legrand, *J. Food Eng.*, 2000, **45**, 195–207.

39 M. Stranzinger, A. Bieder, K. Feigl and E. Windhab, *J. Food Process Eng.*, 2002, **25**, 159–187.
40 J. E. Jorgensen and J. L. Garbini, *J. Fluids Eng.*, 1974, **96**, 158–167.
41 P. Flaud, A. Bensalah and P. Peronneau, *Ultrasound Med. Biol.*, 1997, **23**, 425–436.
42 M. Kagiyama, Y. Ogasawara, S. Tadaoka and F. Kajiya, *Ultrasound Med. Biol.*, 1999, **25**, 1265–1274.
43 N. Müller-Fischer, H. Bleuler and E. J. Windhab, *Chem. Eng. Sci.*, 2007, **62**, 4409–4419.
44 C. Chen, C. Chong, H. Ghazali and O. Lai, *Food Chem.*, 2007, **100**, 178–191.
45 M. H. M. Buscato, R. Grimaldi and T. G. Kieckbusch, *J. Food Sci. Technol.*, 2017, **54**, 3260–3267.
46 S. Yener and H. J. van Valenberg, *Talanta*, 2019, **204**, 533–541.
47 F. Peyronel, B. Quinn, A. G. Marangoni and D. A. Pink, *J. Phys.: Condens. Matter*, 2014, **26**, 464110.
48 E. Vignati, R. Piazza and T. P. Lockhart, *Langmuir*, 2003, **19**, 6650–6656.
49 D. Z. Gunes, M. Murith, J. Godefroid, C. Pelloux, H. Deyber, O. Schafer and O. Breton, *Langmuir*, 2017, **33**, 1563–1575.